The Astrophysical Journal, 994:39 (8pp), 2025 November 20
https://doi.org/10.3847/1538-4357/ae17b3

After 54 Yr of Bar Instability Studies: A Fresh Surprise

J. A. Sellwood[1], Victor P. Debattista[2], and R. G. Carlberg[3]
[1] Steward Observatory, University of Arizona, 933 Cherry Avenue, Tucson, AZ 85722, USA; sellwood@arizona.edu
[2] Jeremiah Horrocks Institute, University of Central Lancashire, Preston, PR1 2HE, UK; vpdebattista@gmail.com
[3] Department of Astronomy and Astrophysics, University of Toronto, Toronto, ON M5S 3H4, Canada; raymond.carlberg@utoronto.ca

Received 2025 September 12; revised 2025 October 21; accepted 2025 October 23; published 2025 November 13

Abstract

The well-known bar instability of rotationally supported disk galaxy models has been studied extensively since its first discovery over half a century ago. We were therefore very surprised to find cases of disks embedded in rigid halos, which on the basis of widely cited criteria should be unstable, that appeared to be robustly stable. Here we show that the unstable bar mode in such simulations was being suppressed by changes to the disk caused by other instabilities having higher angular symmetry that were the first to saturate. Although this may seem like a promising solution to the long-standing puzzle presented by the apparent stability of real disk galaxies, we also show that instability is restored in the same models when the rigid halo is replaced by a live population of particles, where the usual stability conditions apply. Our study has been confined to a narrow range of models, and we cannot therefore exclude the possibility that mode interference may be able to prevent bar formation in other models having live halos.

Unified Astronomy Thesaurus concepts: Spiral galaxies (1560)

1. Introduction

F. Hohl (1971) presented perhaps the first careful simulations that revealed the tendency for disk galaxy models to undergo a global instability that rearranged a rotationally supported disk of stars into a strongly barred configuration. Soon thereafter J. P. Ostriker & P. J. E. Peebles (1973) suggested that the survival of nearly axisymmetric disk galaxies may require them to be embedded in a halo of dark matter, provoking many follow-up studies in both theory (e.g., T. A. Zang 1976, A. J. Kalnajs 1978, A. Toomre 1981) and numerical work (e.g., F. Combes & R. H. Sanders 1981, D. M. Christodoulou et al. 1995, E. Athanassoula & A. Misiriotis 2002, V. P. Debattista et al. 2004) that has continued to this day (e.g., J. A. Sellwood & R. G. Carlberg 2023, hereafter SC23). Despite all these studies, we still lack a widely accepted explanation for the apparent stability of isolated disk galaxies.

It is to be hoped that we may one day identify the explanation for which galaxies do or do not host bars from galaxy formation simulations. These massive experiments (see R. Feldmann & R. Bieri 2026 for a review), which mimic many physical processes, are increasingly able to synthesize somewhat realistic model disk galaxies, especially those of Milky Way mass, but the fraction of these models that support bars, and their properties, varies widely between the different codes that are employed (e.g., D. G. Algorry et al. 2017; D. Zhao et al. 2020; J. Reddish et al. 2022; Y. Rosas-Guevara et al. 2022; S. R. Anderson et al. 2023; S. Ansar et al. 2024; F. Fragkoudi et al. 2025; S. Lu et al. 2025). Though studies of isolated galaxies have provided helpful guidance on the evolution of bars (e.g., S. Ansar et al. 2024), the very complexity of the physical processes in the cosmological context has thus far left the experimenters (e.g., Z.-B. Zhou et al. 2020; S. Ansar et al. 2024) conceding that they are unable to identify the mechanism or properties—star formation and feed back, disk/halo mass fractions, tidal encounters, mergers, etc.–that caused a particular galaxy model to host a bar. Both the algorithms and computer power continue to improve, which it is hoped will eventually enable this question to be answered. In the meantime we pursue a parallel investigation using idealized models in which we have some hope of developing deeper insight into this complicated question of disk dynamics.

G. Efstathiou et al. (1982, hereafter ELN) undertook a systematic study of a family of galaxy models having an exponential disk of mass M_d and radial scale length R_d embedded in various rigid halos and reached the widely cited conclusion that the disk could avoid forming a bar only if the maximum rotational velocity of the disk material $V_m \gtrsim 1.1(GM_d/R_d)^{1/2}$. Since the maximum circular speed due to the disk alone is $\sim 0.62(GM_d/R_d)^{1/2}$ (K. C. Freeman 1970), they argued that stable galaxies must be embedded in massive halos to make up the required circular speed.

The surprise we report here (Section 2) is counterexamples that violate their stability criterion for a reason that, to our knowledge, has not previously been identified: changes to the equilibrium disk caused by saturation of faster-growing spiral modes that disturbed the incipient bar-forming mode, halting its linear growth at an early stage. The apparently stable models were reruns of some of those simulated by SC23, but which included force terms from multiple sectoral harmonics. As a result of our discovery, we were greatly concerned that the principal finding from SC23, that all their models were bar unstable, suddenly appeared to be incorrect because it had been based on simulations that were restricted to $m = 2$ only disturbance forces.

Suppression of bars by prior saturation of competing modes may seem like a promising solution to the bar-instability problem highlighted by J. P. Ostriker & P. J. E. Peebles (1973) and ELN. However, we further report here that the apparent stability of our particular disk galaxy models is a numerical artifact resulting from employing rigid halos. Replacing the rigid halo by a similar one composed of mobile particles allowed the disk to form a strong bar, as expected. While this finding suggests that almost all the models studied by SC23 were indeed unstable, as they had claimed, it does not rule out the possibility that disks in other live halo models could be stabilized by similar nonlinear changes by faster-growing modes.

2. Models and Methods

2.1. Rigid Halo Models

The two galaxy models we employ in this section were selected from the set used by SC23. The exponential disk has the surface density profile

$$\Sigma(R) = \Sigma_0 e^{-R/R_d} \quad \text{with} \quad \Sigma_0 = \frac{M_d}{2\pi R_d^2}, \tag{1}$$

where R_d is the disk scale length and M_d is the nominal mass of the infinite disk. We limit its radial extent using a cubic function to taper the surface density from $\Sigma(5R_d)$ to zero at $R = 6R_d$.

The rotation curve is that of a cored isothermal sphere:

$$V_c(R) = V_0\left[\frac{R^2}{R^2 + r_c^2}\right]^{1/2}, \tag{2}$$

with r_c being the core radius. The implied halo density is whatever is required, when combined with the disk attraction, to achieve this rotation curve in the disk plane (S. M. Fall & G. Efstathiou 1980). We relate the rotation curve to the disk properties by setting $V_0 = 0.9(GM_d/R_d)^{1/2}$ and choose $r_c = R_d/2$ for model A, as the baseline model of SC23, and $r_c = R_d$ for model B. Though quite heavy, the disk has less than the required mass to account for the central attraction at all radii. SC23 reported that these two, and nearly all other models in their study, possessed vigorous, global bar instabilities.

As usual, we adopt units that $G = M_d = R_d = 1$, so a dynamical time is $(R_d^3/GM_d)^{1/2}$, etc. For those who prefer physical units, one possible scaling is to choose $R_d = 2.5$ kpc and the dynamical time to be 10 Myr, which implies $M_d = 3.47 \times 10^{10}\ M_\odot$ and a velocity unit $(GM_d/R_d)^{1/2} = 244.5\ \text{km s}^{-1}$.

SC23 employed the method proposed by F. H. Shu (1969), with numerical details given in J. A. Sellwood (2014), to create an equilibrium distribution function (DF) for the disk particles, which for both models had $Q = 1.2$ at all radii. The sense of net rotation in all models presented in SC23 was positive at all radii, but those authors avoided a discontinuity in the DF by flipping the sign of L_z for a small fraction of low L_z particles.

2.2. 2D Simulation Codes

We select particles from the adopted DF using the procedure described in J. A. Sellwood (2024), place them in a plane at random azimuths (i.e., a noisy start; see Section 2.3 below), and compute the mutual attractions of the particles using either a 2D polar, or a 2D Cartesian, mesh. This code is described in detail in J. A. Sellwood (2014); in summary, the particles move subject to forces from other particles that are interpolated from the grid. We adopt the parameters listed in Table 1.

Table 1
Default Numerical Parameters for our 2D Simulations, the Last Four of Which are Independent of the Grid Type

	Polar Grid	Cartesian Grid
Grid points	171×256	1024×1024
Scaling to grid units	$R_d = 10$	$R_d = 80$
Active sectoral harmonics	$1 \leqslant m \leqslant 8$	unrestricted
Plummer softening length	$\epsilon = R_d/20$	...
Number of particles	6×10^6	...
Largest time step	$0.2R_0/V_0$	...
Radial time step zones	5	

In the polar grid simulations we report in this section, the central attraction is that of a rigid halo needed to ensure centrifugal balance $a_R = -V_c(R)^2/R$, and we neglect the axisymmetric part of the attraction from the mobile particles. We also generally suppress sectoral harmonics $m > 8$ from the force determination, which would add only noise, and describe forces from the active components $1 \leqslant m \leqslant 8$ as "unrestricted," but we also report results from some simulations in which nonaxisymmetric forces were restricted to $m = 2$ only. We include all force terms from the Cartesian grid and supplement the central attraction to maintain the same rotation curve. We employ block time steps that are decreased by factors of 2 in each radial zone.

As usual, we measure nonaxisymmetric distortions of the distribution of the N disk particles using an expansion in logarithmic spirals:

$$A(m, \gamma, t) = \frac{1}{N}\sum_{j=1}^{N}\exp[im(\phi_j + \tan\gamma \ln R_j)], \tag{3}$$

where (R_j, ϕ_j) are the polar coordinates of the jth particle at time t, m is the sectoral harmonic and γ is the (radially constant) angle of the spiral component to the radius vector, which is the complement to the spiral pitch angle.

2.3. Noisy and Quiet Starts

Random selection of the initial particle coordinates from the desired distributions creates an initial model in which density fluctuations are caused by undiminished shot noise arising from the finite number of particles. Evolving such a "noisy start" model with unrestricted forces allows all possible modes, both neutral and unstable, to develop simultaneously.

J. A. Sellwood (1983) described how to create a "quiet start," in which particles are placed almost perfectly symmetrically on rings and given identical orbital and radial velocities. If nonaxisymmetric disturbance forces are also restricted to a single sectoral harmonic the forces experienced by the particles are those from a smooth, massive ring that distorts as expected from growing large-scale disturbances, while the initial regular arrangement inhibits small-scale disturbances. These tricks reduce the level of shot noise by many orders of magnitude and enable identification of linear instabilities that emerge and grow through several e-folds before saturating. See J. A. Sellwood (2024) for more details.

2.4. A Noisy Start Simulation

Figure 1 shows the evolution of a noisy start version, with sectoral harmonics $1 \leqslant m \leqslant 8$ all active, of model A, which is

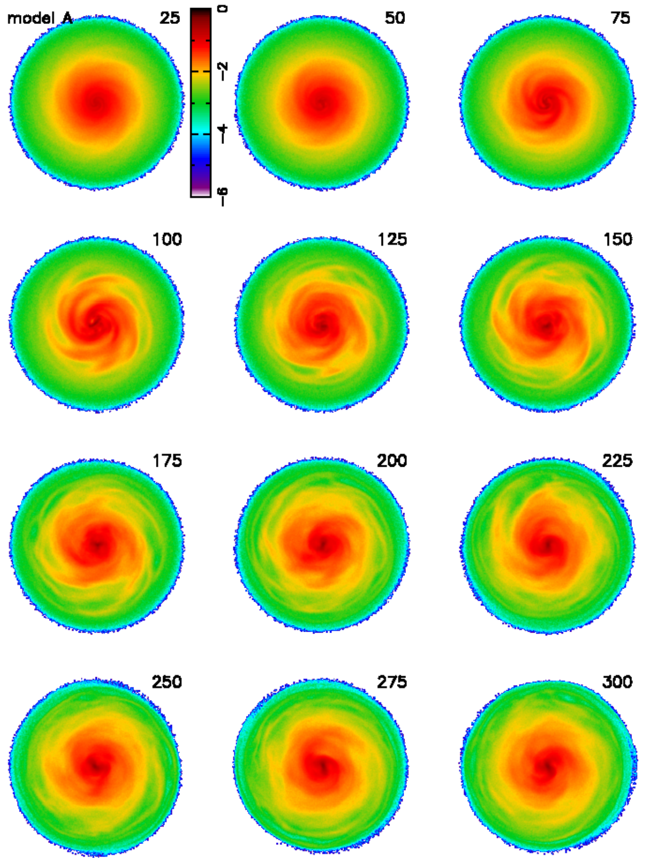

Figure 1. The evolution of a noisy start realization of the baseline model from SC23 with force terms $1 \leqslant m \leqslant 8$ all active. The color scale indicates the logarithm of the disk surface density. Notice that no strong bar forms, though a short, weak bar is visible from time to time.

the baseline model described in SC23. The disk manifested multiarm spiral patterns but did not form a bar.

This figure is to be compared with Figure 3 of SC23, which revealed that the $m = 2$ only, quiet start version of the same model that started from the same file of particles formed a large, strong bar. Note that the e-folding time of the dominant $m = 2$ mode reported in SC23 is ∼32 dynamical times or $\lesssim 1/9$ of the interval illustrated in Figure 1, which is ample for the bar to have emerged from the noisy start if the same mode had saturated in this new simulation.

We have verified that a rerun of the same model using a Cartesian grid with unrestricted forces did not form a bar either, and its evolution closely resembled that illustrated in Figure 1.

It has long been known (e.g., J. A. Sellwood & R. G. Carlberg 1984) that spiral activity heats the disk and causes the spirals to fade over time. Figure 2 presents the time evolution of the radial Q profile in model A, revealing a rise to $Q \gtrsim 2.3$ over the range $1 \leqslant R \leqslant 4$ and still higher at larger radii. Heating of the very inner disk was largely suppressed by the high density of the inner halo.

2.5. Comparison with ELN

The pioneering simulations by ELN were similar in almost all respects to the noisy start model illustrated here as Figure 1, except that the limited computational power available at the time forced them to employ merely 2×10^4 particles and a 2D grid that had 128^2 cells. From these crude, by today's standards, simulations, they concluded that bars always formed provided $V_0 \lesssim 1.1$ (Equation (2)). We note that our simulation illustrated in Figure 1 had $V_0 = 0.9$. A noisy start simulation of our model B, which also had $V_0 = 0.9$ but the larger core radius $r_c = R_d$, did not form a strong bar either, and this model had exactly the same properties as model 11 in the paper by ELN. Those authors concluded from the slow decline of their δ_2 parameter (bottom, middle panel of their Figure 2) that their model 11 was bar unstable.

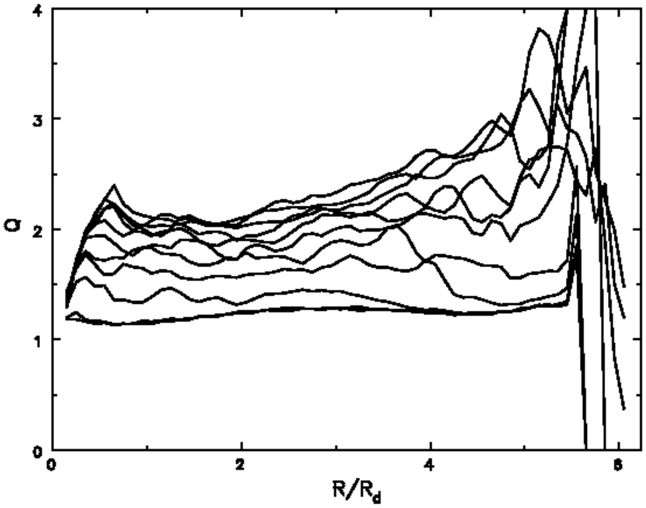

Figure 2. The radial variation of Q at intervals of 50 dynamical times in the simulation illustrated in Figure 1. The lines are not labeled because increases in Q are mostly monotonic.

Neither of our noisy start simulations of models A and B, with $V_0 = 0.9$, formed bars, which is in violation of the widely cited stability criterion proposed by ELN. In order to investigate the cause of this discrepancy, we have run a further 79 separate simulations of model A, in which we employed four differing numbers of particles, each with 10 different random seeds used to select the initial particle coordinates, and finally we computed all 40 models twice, once with forces from sectoral harmonics $1 \leqslant m \leqslant 8$ all active and again with $m = 2$ forces only. Figure 3 illustrates the evolution of one case: the strong $m = 3$ spiral pattern that is already visible at $t = 25$ is typical of all our low-N simulations having unrestricted forces.

Each line in each panel of Figure 4 presents the time evolution of the given logarithmic spiral amplitude, averaged over the minor stochastic differences between 10 realizations having different random seeds, and the four lines in each panel span a factor of 1000 in the values of N.

The simulations in the top two panels employed unrestricted forces, and we report the amplitude of the bar-like $A(2, 0)$ and the trefoil $A(3, 0)$ coefficients in the top and middle panels, respectively. Amplitudes are largest in the smallest N simulations (red curves) at early times, reflecting the higher level of seed noise, but there is no evidence that the amplitudes at later times depend on the number of particles employed. The final bar amplitudes are $A(2, 0) \sim 0.02$, which is very weak, and $A(2, 0) \gtrsim 0.12$ for strong bars (e.g.,, J. A. Sellwood & E. Athanassoula 1986; SC23). Notice also that the $m = 3$ coefficients decrease somewhat over time, perhaps exceeding those of $m = 2$ at first but ending slightly smaller. The behavior of the red line in the top panel ($m = 2$) resembles the evolution of the similar δ_2 parameter presented by ELN in their Figure 2 for their low-N simulation, despite the different scaling.

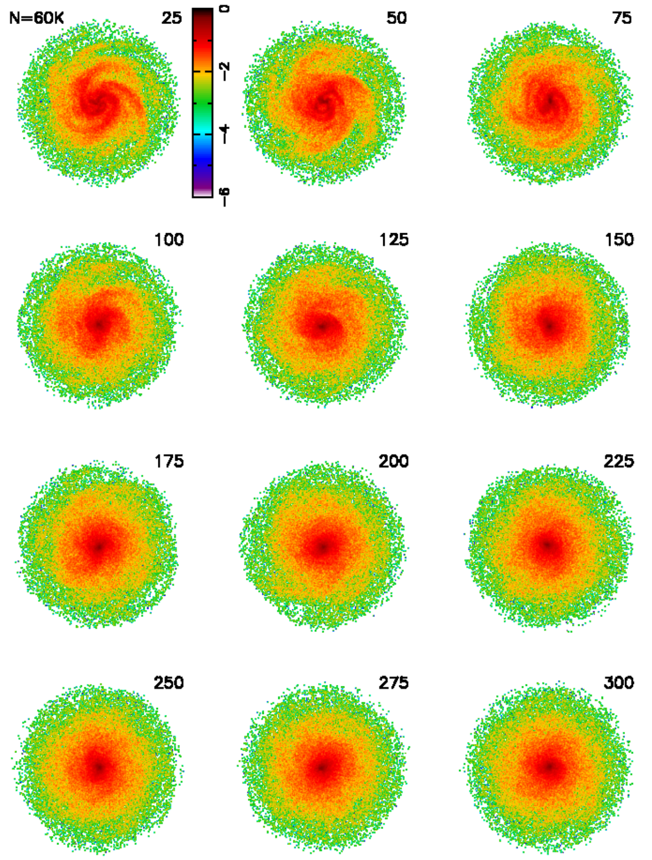

Figure 3. The evolution of one comparison simulation of model A having $N = 60\mathrm{K}$ particles. The initial disk extends to $R = 5R_d$, and times are given in dynamical times.

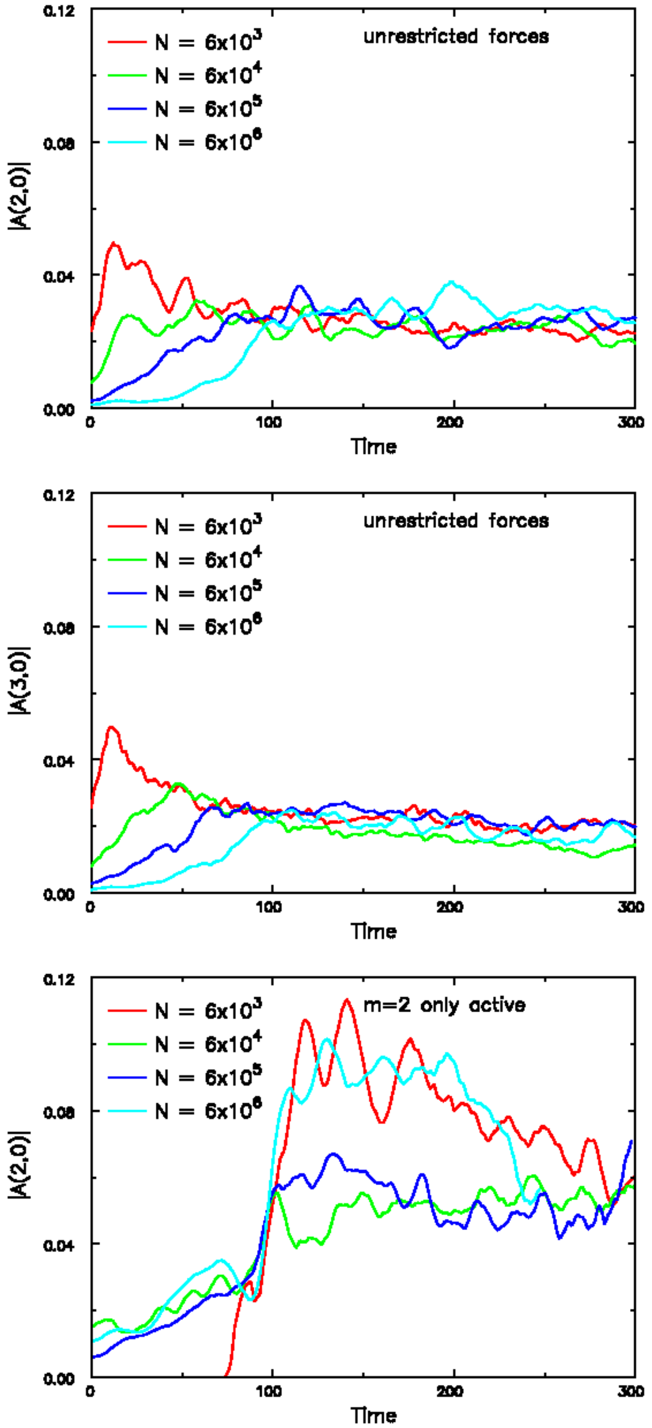

Figure 4. Top: the mean amplitudes of the bar-like $A(2, 0, t)$ (Equation (3)) in 10 noisy start realizations of model A for four different values in N with unrestricted forces. Middle: the same as for the top panel but for $m = 3$. Bottom: the evolution of the bar amplitude in identical noisy start simulations when nonaxisymmetric forces are restricted to $m = 2$. Results from the individual simulations were shifted in time in the bottom panel only so that $A = 0.06$ at $t = 100$ for each before averaging.

The bottom panel of Figure 4 reports results from a separate set of simulations starting from the same files of particles as those in the top two panels, but in which we restricted nonaxisymmetric forces to the $m = 2$ sectoral harmonic only. As we suspected that a dominant bar-forming mode was present in these runs (as found by SC23) we attempted to align the amplitude variation to pass through $A = 0.06$ at $t = 100$ in each separate simulation before averaging so that time offsets between the separate cases did not obscure the trends. This strategy was moderately successful, and it is apparent that bars in these models have much greater amplitude than in the top panel, a clear indication that nonlinear interference from modes having other symmetries inhibited the bar instability.

We followed up this hint by conducting other quiet start simulations of model A with disturbance forces restricted to $m = 3$ or $m = 4$ to search for other linear instabilities, finding one $m = 4$ mode whose growth rate was only slightly lower than that of the dominant $m = 2$ mode and two three-fold symmetric modes having growth rates that exceeded it. All these, and probably other, modes would have started to grow from the outset of the simulation illustrated in Figure 1. Multiple spiral arms can be seen in this figure as early as $t = 100$, when the condition for independent linear growth of each mode is clearly no longer satisfied.[4] We therefore conclude that the bar instability can be inhibited by nonlinear changes caused by other modes, provided they disturb the inner disk before the bar-forming instability saturates. We describe more fully what we mean by this statement in Section 2.6.

Before this study, we were unaware of the rapidly growing additional $m = 3$ and $m = 4$ modes that saturated before the bar mode, inhibiting the large bar that developed in simulations only when disturbance forces are restricted to

---

[4] Namely that for as long as nonaxisymmetric distortions and changes to particle velocities continue to be negligible.

$m = 2$. Our resimulations of a few of the models from ELN with $N = 2 \times 10^4$ particles and 128^2 Cartesian grid, and also with the polar grid, possessed $m = 3$ features that were stronger than those of $m = 2$ in the early evolution (see also Figure 3), but the relative amplitudes of the two sectoral harmonics were reversed after $t \sim 100$, consistent with the persistence of $m = 2$ reported by ELN, which evidence may have formed the basis for their stability criterion.

2.6. Technical Discussion

Linear instabilities (see, e.g., J. A. Sellwood & K. L. Masters 2022 for a fuller discussion) grow exponentially for as long as the amplitude of every disturbance is small enough that terms in the collisionless Boltzmann equation (CBE) that are second order in the perturbation amplitude can be neglected. Once this assumption breaks down, the dominant mode is said to saturate; the neglected terms in the CBE begin to cause finite changes to the initial equilibrium model, and its exponential growth ceases. The changes to the equilibrium model are largest at the principal resonances of the mode (D. Lynden-Bell & A. J. Kalnajs 1972) and alter both the angular momenta of the affected particles and, at the Lindblad resonances only, increase their random energy, which is the reason that the nonlinear evolution of spiral instabilities causes disks to heat, as shown in Figure 2 (see also J. A. Sellwood & R. G. Carlberg 2019; M. Roule et al. 2025). Stars that lose angular momentum at corotation as a vigorous bar-forming mode saturates, on the other hand, become trapped into a tumbling bar, while gainers at this resonance move to larger orbits.

The initial amplitude of each mode is determined by the spectrum of shot noise from the coordinates of each particle. Thus changing the random seed used for the initial positions of each particle will change the initial amplitude of every mode, although each will again start to grow at the rates of the separate linear modes. If, as here, there are several instabilities having comparable growth rates, the mode that saturates first could differ between runs having different random seeds, leading to macroscopic stochastic differences in the later evolution (see J. A. Sellwood & V. P. Debattista 2009 for an in depth study). It seemed possible that the absence of a large bar in Figure 1 could be a consequence of an unlucky random seed, but this idea was ruled out by the results presented in the top panel of Figure 4. Not one of the 10 randomly seeded models at each N formed a strong bar.

In the case of the simulations reported by ELN, in which multiple instabilities saturate in quick succession, some trapping into a bar could perhaps start to occur at about the same time as the disk is being heated by spiral modes. When resonances of separate large-amplitude modes overlap, the dynamics can become chaotic (K. J. Daniel & R. F. G. Wyse 2018), made more so by the changing amplitudes of both disturbances in this case. Lindblad resonance scattering by a spiral mode may inhibit some of the trapping that would have occurred if the bar mode had been isolated, leading to a much weaker bar as the model settles after these events. Indeed, ELN's measurements of their parameter δ_2 are surprisingly small compared with those for bar instabilities uncontaminated by competing spiral modes (e.g., J. A. Sellwood & E. Athanassoula 1986).

The linear growth rates of all modes should be the same regardless of the particle number, but as noted above, the seed amplitudes of all modes in ELN's simulations would have been much higher than those in our $N = 6$ million particle models. Therefore the modes would have saturated much sooner after the start, leaving little time for the small differences in growth rates to matter.

The situation is cleaner when the times of saturation of the separate modes are well spaced, as occurred in our model shown in Figure 1. Some spiral modes grow more rapidly than does the bar mode, and therefore the equilibrium disk in which the bar mode is growing linearly can suddenly be altered by the nonlinear heating caused by a spiral instability. It would be difficult to predict the outcome of this event, but the absence of even a vestige of a large bar in our simulation indicates that the linear growth of the bar-forming instability is terminated at small amplitude before any trapping occurs.

The corotation radius of the bar instability in model A is $\sim$2.1, while the outer Lindblad resonances of the faster-growing $m = 3$ modes mentioned above are at $R \sim 1.80$ and $\sim$1.93. Thus, while the exponentially growing bar instability was still at small amplitude, these, and possibly other, spiral modes will have saturated and heated the disk at their Lindblad resonances (D. Lynden-Bell & A. J. Kalnajs 1972), thereby changing the properties of the disk near corotation of the bar mode during its linear growth. This interference apparently killed off the bar-forming mode because no bar developed in Figure 1.

3. Live Halo Models

It has long been known (E. Athanassoula 2002; K. Saha & T. Naab 2013; J. C. Berrier & J. A. Sellwood 2016) that a live halo provides a supporting response to the bar instability in a disk, causing that mode to grow more rapidly than in the equivalent rigid halo. The open spiral of the bar mode couples strongly to those bisymmetric orbits in the halo that precess at similar rates to those in the disk, especially any whose orbit planes are not far from the disk plane (J. A. Sellwood 2016). Thus the instability is that of the combined halo+disk system, which a rigid halo could not capture.

In order to study the stability of a disk embedded in a live halo, it is necessary first to create an equilibrium model. However, it would be extremely difficult to create live halo versions of the family of simple models adopted by ELN, since the halo density in any one model does not have a simple form. Their models specify an attractively simple functional form for the total rotation curve (Equation (2)), which results from the combined attraction of the disk and halo. The attraction of a thin exponential disk can be expressed in terms of modified Bessel functions (K. C. Freeman 1970), but the attraction of the halo must be that which would result from the total radial attraction, $V_c^2(R)/R$, with the disk contribution subtracted. While the required halo attraction could be calculated numerically, it clearly would not have a simple functional form. Note that not all possible models would be physically acceptable since a heavy disk embedded in a halo having a large core radius r_c could require the halo density to be negative at some radii.

Possible methods that could be employed to construct an equilibrium DF for the halo having an embedded disk are as follows:

1. E. Vasiliev (2018) proposed the AGAMA procedure to create an equilibrium disk+halo model in any one case. However, one must choose a function of the actions, and the method converges to an equilibrium model by

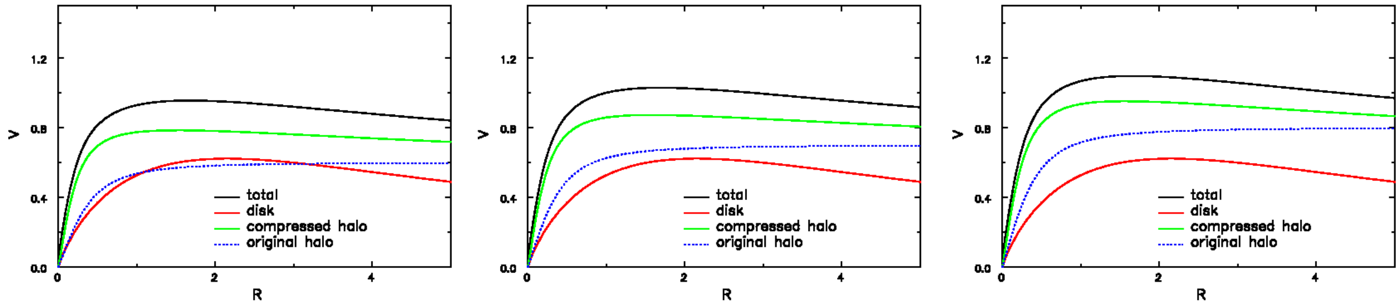

Figure 5. Three example rotation curves (black curves) of disk + compressed halo. The disk contribution, which is the same in all three, is shown in red and the compressed halo in green, with $V_0 = 0.6$ in the left panel, $V_0 = 0.7$ in the middle panel, and $V_0 = 0.8$ in the right panel. In all three panels the contribution of the halo before compression, for which $r_c = R_d/2$, is shown by the dotted curve.

iteration, making it hard to achieve exactly the desired disk/halo mass ratio and rotation curve.

2. A second option, adopted by K. Holley-Bockelmann et al. (2005), is to use Eddington inversion to find an equilibrium DF for a halo having an embedded disk. The inversion formula requires both the halo density and the total central attraction of the halo and disk (assumed spherical). One must check that the resulting isotropic DF is positive over the entire energy range, as inversion (also described by J. Binney & S. Tremaine 2008) does not guarantee that it is.
3. A third possible procedure, which we prefer here, is to use halo compression. One starts with a simple halo model having a known DF and computes a revised DF after the disk is added, assuming the potential change caused by adding the disk was adiabatic. The method was pioneered by P. Young (1980), who used the fact that the DF, expressed as a function of the actions, is invariant during an adiabatic change to the potential. The two actions in a perfectly spherical model are angular momentum and radial action. J. A. Sellwood & S. S. McGaugh (2005) describe the calculation details for the case of a halo+disk. As for Eddington inversion, the attraction of the disk must be assumed spherical, but J. A. Sellwood & S. S. McGaugh (2005) showed this was an excellent approximation. Even if the DF before compression was isotropic, inserting a disk and/or bulge gives the compressed DF a mild radial bias.

In addition to being adaptable, halo compression is guaranteed to yield a physically acceptable model in which the density remains positive everywhere. Moreover, the iteration quickly converges to the equilibrium model, and therefore the precompression model can be tweaked if the postcompression model is not to one's liking.

3.1. Halo+Disk Models

Here we adopt the cored isothermal sphere for the precompression halo, which has the radial density profile

$$\rho(r) = \frac{V_0^2}{4\pi G r_c^2}\frac{3 + x^2}{(1 + x^2)^2}, \qquad (4)$$

where $x = r/r_c$, with r_c being the core radius, and V_0 the asymptotic circular speed when $x \gg 1$. An isotropic DF for this mass profile is readily determined by Eddington inversion.

We truncate this infinite mass halo by limiting the maximum apocentric distance of any orbit to be r_t. Thus the maximum allowed energy of an orbit of total angular momentum L is $E_{\max} = \Phi(r_t) + (L/r_t)^2/2$, with $\Phi(r) = (V_0^2/2)\ln(1 + x^2)$ being the gravitational potential of the halo before the addition of a disk.

Table 2
Numerical Parameters for our 3D Simulations

	Cylindrical Grid	Spherical Grid
Grid size	(N_R, N_ϕ, N_z) $=(170, 256, 125)$	... $n_r = 201$
Angular components	$0 \leqslant m \leqslant 8$	$0 \leqslant l \leqslant 4$
Outer radius	$6.30R_d$	$45R_d$
z-spacing	$0.025R_d$	...
Softening rule	cubic spline	none
Softening length	$\epsilon = 0.05R_d$	...
Number of particles	6×10^6	5×10^6
Longest time step	$0.1(R_d^3/GM)^{1/2}$	...
Time step zones	5	...

We insert the exponential disk (Equation (1)) whose center coincides with the center of the halo and compute the resulting rotation curve of the combined equilibrium model. Some examples are shown in Figure 5.

3.2. Evolution of a Live Halo Model

We select the model shown in the left panel of Figure 5, which has a total rotation curve that approximates that of our model A, and evolve it using our hybrid grid method. The disk particles are assigned to a 3D polar grid, while the field of the halo particles is computed using a multipole expansion on the spherical grid, as is fully described in J. A. Sellwood (2014). Our chosen values for the numerical parameters are given in Table 2.

The evolution of the disk component of this model having a live halo, which forms a strong bar by $t \sim 150$, is presented in Figure 6. This contrasts with the model shown in Figure 1, which had a very similar (but not identical) rigid halo. As has been found previously, the live halo encourages the formation of the bar.

Figure 7 gives the amplitude evolution of the bar-like logarithmic spiral component (Equation (3)) of this and two additional simulations having heavier halos, also shown in Figure 5. That with $V_0 = 0.7$ for the uncompressed halo also formed a bar, while only multiarm spirals and no bar formed in the model having the still heavier halo with $V_0 = 0.8$.

The left panel of Figure 8 reports the angular momenta of the separate disk and halo components in these three

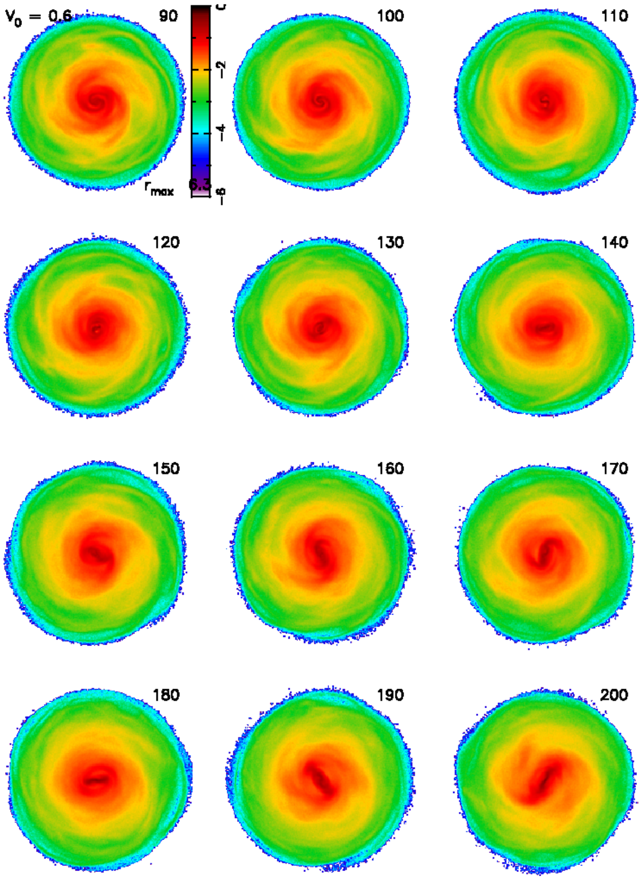

Figure 6. The later part of the evolution of the disk component in the $V_0 = 0.6$ 3D simulation, whose rotation curve is given in the left panel of Figure 5. Notice that a strong bar forms.

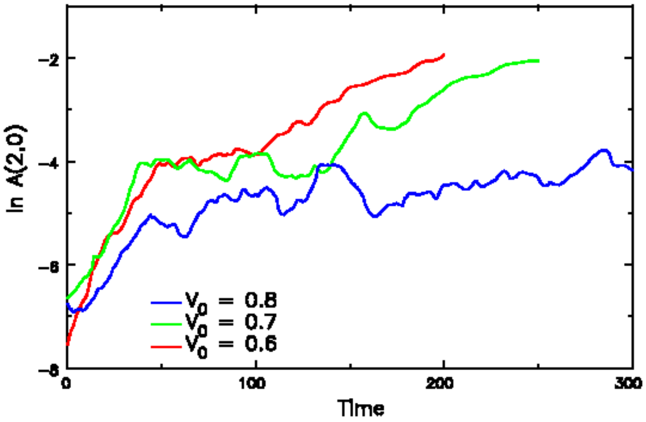

Figure 7. The amplitude evolution of the bar-like logarithmic spiral component in the disks of three simulations having different compressed live halos.

simulations, while the right panel gives the torque acting on the halo in all three cases. The angular momentum taken from the disk is the time integral of the torque, which is very small in the case of the densest halo (blue lines). The formation of a bar is associated with angular momentum transfer to the halo, as has been reported before (J. A. Sellwood 2016).

In light of our experience reported in Section 2 above, we zeroed out all bisymmetric force terms on both grids and reran the simulation illustrated in Figure 6 to search for possible more slowly growing instabilities but found none. Thus the question of possible mode interference in this live halo model does not arise.

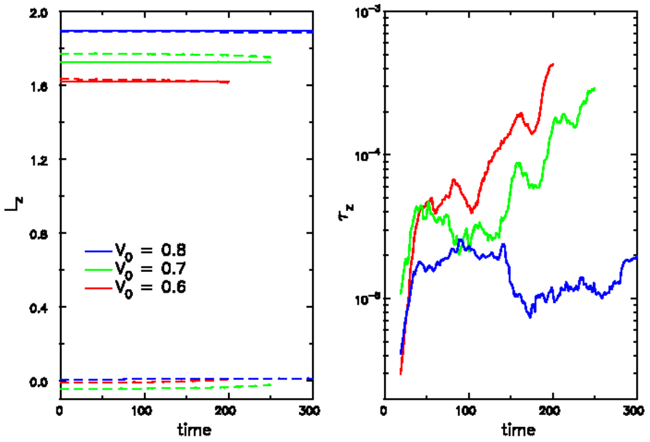

Figure 8. The dashed lines in the left panel indicate the separate angular momenta of the disks and halos, while the solid lines are their sum, demonstrating that this global integral is well conserved. The right panel gives the rates at which angular momentum is taken from the disk component and added to the halo.

3.3. Disk Stability

The black curves in Figure 5 indicate $V_{c,max} \simeq 1.10$ for the bar-stable model in the right-hand panel and $V_{c,max} \simeq 1.03$ for the bar-unstable model in the middle panel.[5] These two results, which are from just two simulations, are consistent with the old stability criterion proposed by ELN, which proposed that models having $V_{c,\max} \gtrsim 1.1$ should be stable. Our finding that the ELN stability criterion, which was derived from 2D simulations in rigid halos, holds in these two cases of 3D disks in live halos was a surprise since E. Athanassoula (2008) argued that it needed to be revised.

A. Toomre (1981) found that the swing amplifier, which drives the bar mode in disks, would die away when its parameter $X \gtrsim 3$. Unfortunately, $X \equiv 2\pi R/m\lambda_{\rm crit}$ is a locally defined parameter, but we find that it has a minimum near $R = R_d$ in our models, where $X_{\rm min} \simeq 2.60$, 3.02, and 3.45 when $V_0 = 0.6$, 0.7, and 0.8, respectively. The $V_0 = 0.7$ model, for which $X_{\rm min} \simeq 3.02$, was unstable, but it is on the boundary given by Toomre for effectiveness of the swing amplifier, and the mild help from halo coupling probably tipped it into instability. The outcomes in the two other cases were also consistent with the predictions of swing-amplifier theory.

4. Conclusions

We have shown that moderately heavy disks embedded in rigid halos can appear to be stable when disturbance forces within the disk plane are unrestricted. This result contrasts both with the findings of SC23 and violates the stability criterion proposed long ago by ELN. We have demonstrated that nonlinear scattering by other modes halts the growth of the bar mode prior to its expected saturation in these models. We were unaware at the time of our earlier study (SC23) that the responsible modes, which have different rotational symmetries, have linear growth rates that are comparable to, or even exceed, that of the bar mode. Since linear perturbation theory

---

[5] Note that $V_{c,\max}$ includes both the compressed halo and disk, while here V_0 is for the uncompressed halo only.

neglects changes to the background disk, the linear growth of a mode is disturbed when the background disk is altered by the saturation of a faster-growing mode, which in our models prevented the incipient bar instability from creating a bar.

The situation is different when disturbance forces are restricted to a single sectoral harmonic, since all modes having other angular symmetries are suppressed, and the dominant mode of the selected rotational symmetry can win out, as was true for all the simulations in SC23.

While the above discussion applies to disks embedded in rigid halos, the stability properties of disks in live halos can differ again because the bar mode elicits a supporting response from the halo even in the linear regime (J. A. Sellwood 2016). We have also shown that a disk that appeared to be stable when embedded in a rigid halo was strongly unstable in a similar halo that was composed of mobile particles. Furthermore, the stability criteria proposed for disks in rigid halos by ELN and by A. Toomre (1981) appear to hold for our three live halo models.

Our discovery that bar-forming modes can be inhibited by faster-growing spiral modes has turned out in this study to be an interesting side issue that ultimately did not affect global stability when simulated with unrestricted disk forces and embedded in live halos. If live halo models having more vigorous spiral modes exist, they may provide an interesting new solution to the long-standing puzzle presented by the bar instability.

Acknowledgments

We thank the referee for a supportive review, thoughtful comments, and for encouraging us to clarify some technical points. J.A.S. acknowledges the continuing hospitality and support of Steward Observatory.

Data Availability

The data from the simulations reported here can be made available on request. The simulation code and analysis software can be downloaded in one bundle from http://www.physics.rutgers.edu/galaxy and is documented in the code manual (J. A. Sellwood 2014).

ORCID iDs

J. A. Sellwood https://orcid.org/0000-0003-2723-2496
Victor P. Debattista https://orcid.org/0000-0001-7902-0116
R. G. Carlberg https://orcid.org/0000-0002-7667-0081

References

Algorry, D. G., Navarro, J. F., Abadi, M. G., et al. 2017, MNRAS, 469, 1054
Anderson, S. R., Gough-Kelly, S., Debattista, V. P., et al. 2023, MNRAS, 527, 2919
Ansar, S., Pearson, S., Sanderson, R. E., et al. 2024, ApJ, 978, 37
Athanassoula, E. 2002, ApJL, 569, L83
Athanassoula, E. 2008, MNRAS: Letters, 390, L69
Athanassoula, E., & Misiriotis, A. 2002, MNRAS, 330, 35
Berrier, J. C., & Sellwood, J. A. 2016, ApJ, 831, 65
Binney, J., & Tremaine, S. 2008, Galactic Dynamics: Second Edition (Princeton, NJ: Princeton Univ. Press)
Christodoulou, D. M., Shlosman, I., & Tohline, J. E. 1995, ApJ, 443, 563
Combes, F., & Sanders, R. H. 1981, A&A, 96, 164
Daniel, K. J., & Wyse, R. F. G. 2018, MNRAS, 476, 1561
Debattista, V. P., Carollo, C. M., Mayer, L., & Moore, B. 2004, ApJL, 604, L93
Efstathiou, G., Lake, G., & Negroponte, J. 1982, MNRAS, 199, 1069
Fall, S. M., & Efstathiou, G. 1980, MNRAS, 193, 189
Feldmann, R., & Bieri, R. 2026, Encyclopedia of Astrophysics (Amsterdam: Elsevier), 576
Fragkoudi, F., Grand, R. J. J., Pakmor, R., et al. 2025, MNRAS, 538, 1587
Freeman, K. C. 1970, ApJ, 160, 811
Hohl, F. 1971, ApJ, 168, 343
Holley-Bockelmann, K., Weinberg, M., & Katz, N. 2005, MNRAS, 363, 991
Kalnajs, A. J. 1978, in IAU Symp. 77, Structure and Properties of Nearby Galaxies, ed. E. M. Berkhuijsen & R. Wielebinski (Dordrecht: Reidel), 113
Lu, S., Du, M., & Debattista, V. P. 2025, A&A, 697, A236
Lynden-Bell, D., & Kalnajs, A. J. 1972, MNRAS, 157, 1
Ostriker, J. P., & Peebles, P. J. E. 1973, ApJ, 186, 467
Reddish, J., Kraljic, K., Petersen, M. S., et al. 2022, MNRAS, 512, 160
Rosas-Guevara, Y., Bonoli, S., Dotti, M., et al. 2022, MNRAS, 512, 5339
Roule, M., Fouvry, J.-B., Pichon, C., & Chavanis, P.-H. 2025, A&A, 699, A140
Saha, K., & Naab, T. 2013, MNRAS, 434, 1287
Sellwood, J. A., & Masters, K. L. 2022, ARA&A, 60, 73
Sellwood, J. A. 1983, JCoPh, 50, 337
Sellwood, J. A. 2014, arXiv:1406.6606
Sellwood, J. A. 2016, ApJ, 819, 92
Sellwood, J. A. 2024, MNRAS, 529, 3035
Sellwood, J. A., & Athanassoula, E. 1986, MNRAS, 221, 195
Sellwood, J. A., & Carlberg, R. G. 1984, ApJ, 282, 61
Sellwood, J. A., & Carlberg, R. G. 2019, MNRAS, 489, 116
Sellwood, J. A., & Carlberg, R. G. 2023, ApJ, 958, 182
Sellwood, J. A., & Debattista, V. P. 2009, MNRAS, 398, 1279
Sellwood, J. A., & McGaugh, S. S. 2005, ApJ, 634, 70
Shu, F. H. 1969, ApJ, 158, 505
Toomre, A. 1981, in Structure and Evolution of Normal Galaxies, ed. S. M. Fall & D. Lynden-Bell (Cambridge: Cambridge Univ. Press), 111
Vasiliev, E. 2018, MNRAS, 482, 1525
Young, P. 1980, ApJ, 242, 1232
Zang, T. A. 1976, PhD thesis, Massachusetts Institute of Technology
Zhao, D., Du, M., Ho, L. C., Debattista, V. P., & Shi, J. 2020, ApJ, 904, 170
Zhou, Z.-B., Zhu, W., Wang, Y., & Feng, L.-L. 2020, ApJ, 895, 92